

Chapter 3

Experimental Techniques

In the context of this thesis, mainly three surface sensitive experimental techniques are used to study different aspects of quasicrystal surfaces. Low-energy electron diffraction (LEED) and elastic Helium atom scattering (HAS) are diffraction methods probing the reciprocal space. These methods provide information about surface symmetries and unit cell dimensions. The third method, low-energy electron microscopy LEEM, images the real space of the surface with a resolution of about 10 nm at video-rate. This allows the study of dynamic processes at the surface in real time, as for example, in situ investigations of temperature induced phase transitions. Additionally, valuable information of the reciprocal space can be obtained from the LEED pattern.

First, the elastic scattering theory common to both electron and helium atom diffraction is discussed. In sections 3.2 and 3.3 experimental details of helium atom scattering and high resolution low energy electron diffraction (SPA-LEED) are presented. The LEEM instrument is introduced in section 3.4 including a brief overview of the contrast mechanisms.

3.1 Elastic Scattering Theory

Scattering of particles from solids is determined by their de Broglie wavelength and the scattering potential. The de Broglie wavelength $\lambda = \sqrt{\frac{h^2}{2mE}}$ of particles with mass m and kinetic energy E amounts to

$$\lambda[\text{\AA}] = \sqrt{\frac{150.4}{E[\text{eV}]}} \quad (3.1)$$

for electrons and

$$\lambda[\text{\AA}] = \sqrt{\frac{20.9}{E[\text{meV}]}} \quad (3.2)$$

for helium atoms. For electron energies between 10 eV and 500 eV and for helium atoms with energies of 10 meV to 100 meV the wavelengths are on the order of inter-atomic distances in solids.

3.1.1 Low Energy Electron Diffraction

The penetration depth of an electron in this energy range is limited to a few atomic layers. Thus, LEED is a surface sensitive technique. To extract information from electron diffraction patterns there are two major methods known as kinematic and dynamic approach: The kinematic theory is an approximation of the complete scattering process as a single scattering event. As a consequence only the diffraction spot positions and their intensity profile $I(\mathbf{k}_{\parallel})$ are analyzed in order to derive basic structural parameters which will be discussed later. In contrast, the dynamic theory accounts for multiple scattering events and involves the total scattering intensity as a function of energy. Thus, conclusions on the atomic distribution within the unit cells can be drawn. The data presented in this thesis are solely analyzed within the kinematic approximation.

3.1.2 Helium Atom Scattering

When helium atoms impinge on a surface they are first attracted by van der Waals forces before they are repelled at about 2-3 Å above the surface due to the overlap of their electronic wave functions with those of the sample (Pauli exclusion principle). In a simple picture the helium atom-surface potential can be described by a Lennard-Jones type as illustrated in figure 3.1. The shape varies along the surface plane [43]. The classical turning point of particles incident on top sites of the surface lies further away than from particles impinging on hollow sites. Thus the line of classical turning points is modulated by the atomic structure of the surface, defining the corrugation function $\zeta(\mathbf{r}_{\parallel})$, where \mathbf{r}_{\parallel} denotes a vector in the surface plane.

In first order approximation the corrugation function corresponds to an equipotential line with constant electronic charge density such that the repulsive part of the atom-surface potential V_{rep} can be written as [44]

$$V_{rep}(r) = \alpha\rho(r) . \quad (3.3)$$

The discrete energy levels in the attractive part of the atom-surface potential open up the possibility of selective adsorption of the impinging He atoms into bound states [46]. In a second step the atom may or may not leave the surface through one of the diffraction channels. Consequently, bound state resonances involve abrupt changes in the elastic scattering intensity when the angle or the energy of the incident He beam are varied.

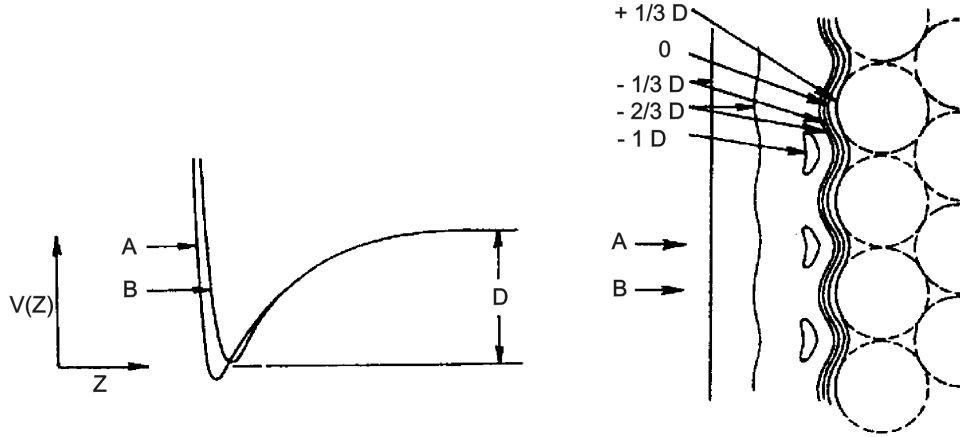


Figure 3.1: Illustration of the helium atom-surface potential [43, 45]. The potential as a function of distance to the surface is of Lennard-Jones type at all position on the sample (left hand side), but varies in shape along the surface plane. The variation is defined by the corrugation function of the surface. The equipotential lines of parameter D , which is the depth of the potential well, are indicated in the right part of the figure.

Due to thermal vibrations of the surface atoms, the corrugation of the surface is modulated in time and inelastic scattering processes may take place by an energy transfer between the incident He atoms and the surface vibrational modes. Although the HAS apparatus is capable of recording phonons by the time-of-flight technique, these were not studied as part of this thesis and therefore will not be discussed.

3.1.3 Kinematic Approximation

Elastic diffraction requires two conditions to be fulfilled. First, conservation of energy, expressed as

$$\mathbf{k}_i^2 = \mathbf{k}_f^2 = \mathbf{k}_{\parallel,f}^2 + \mathbf{k}_{f,z}^2 \quad (3.4)$$

and, second, parallel momentum conservation

$$\mathbf{k}_{\parallel,i} + \mathbf{G} = \mathbf{k}_{\parallel,f} . \quad (3.5)$$

In the two equations \mathbf{k}_i and \mathbf{k}_f are the initial and final wave vectors of the scattered particle, and \mathbf{G} is an arbitrary reciprocal lattice vector. Equation 3.5 therefore states the Bragg condition.

The diffraction of particles from a surface can be described by the sum of the electron waves scattered from the incident wave vector \mathbf{k}_i into the final wave vector \mathbf{k}_f by all surface atoms at

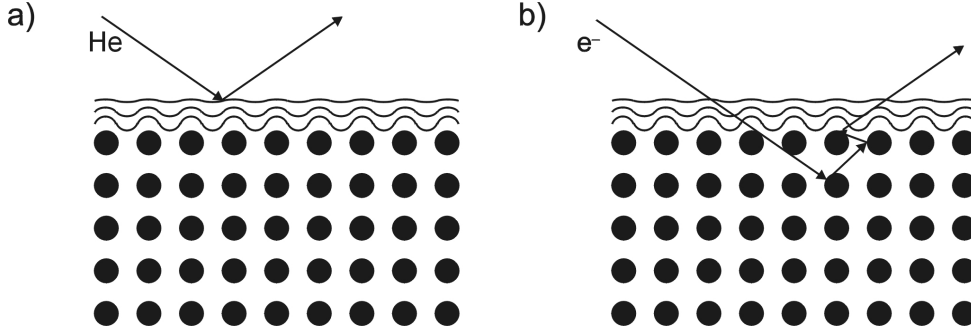


Figure 3.2: Comparison of Helium and electron scattering from solid surfaces. (a) Helium atoms are reflected above the surface, while (b) low energy electrons penetrate a few atomic layers into the surface.

positions \mathbf{r}_n .

$$\psi(\mathbf{k}, \mathbf{k}_i) = \sum_n f_n(\mathbf{k}, \mathbf{k}_i) e^{i\mathbf{k}\mathbf{r}_n} = S(\mathbf{k}, \mathbf{k}_i) \quad (3.6)$$

with $\mathbf{k} = \mathbf{k}_i - \mathbf{k}_f$ the scattering vector, $f_n(\mathbf{k}, \mathbf{k}_i)$ the form factor and

$$S(\mathbf{k}, \mathbf{k}_i) = \sum_n f_n(\mathbf{k}, \mathbf{k}_i) e^{i\mathbf{k}\mathbf{r}_n} \quad (3.7)$$

the structure factor. Hence, the diffraction spot intensity written as

$$I(\mathbf{k}, \mathbf{k}_i) = |\psi(\mathbf{k}, \mathbf{k}_i)|^2 = S^*(\mathbf{k}, \mathbf{k}_i) S(\mathbf{k}, \mathbf{k}_i) \quad (3.8)$$

$$= \sum_{n,m} f_m(\mathbf{k}, \mathbf{k}_i) f_n^*(\mathbf{k}, \mathbf{k}_i) e^{i\mathbf{k}(\mathbf{r}_n - \mathbf{r}_m)} \quad (3.9)$$

is dependent on the structure factor, and consequently on the form factor, i.e., on the scattering power of the atoms.

Since the helium atoms are reflected above the surface, only the outermost layer interacts with the incident particles. As the corrugation $\zeta(\mathbf{r}_{\parallel})$ describes the scattering potential, the scattering centers are continuously distributed along $\zeta(\mathbf{r}_{\parallel})$ [47]. If the corrugation is a shallow function a single scattering event and equivalent form factors f_n distributed along the corrugation can be assumed. Hence, the structure factor $S(\mathbf{k}, \mathbf{k}_i)$ in equation 3.7 transforms into [47]

$$S(\mathbf{k}, \mathbf{k}_i) = \frac{1}{g} \int e^{i(\mathbf{G}\mathbf{r}_{\parallel} + (k_{fz} - k_{iz})\zeta(\mathbf{r}_{\parallel}))} d\mathbf{r}_{\parallel} \quad (3.10)$$

where k_{fz} and k_{iz} denote the z -component of the final and incident wavevector, respectively. The factor $1/g$ accounts for the normalization such that the total outgoing flux is equal to the incoming flux of the helium atoms. Equation 3.10 is the so-called eikonal formula. Since there is no strict selection rule for \mathbf{k}_{\perp} , the probed reciprocal space consists of lattice rods whose intensity is weakly modulated dependent on $S(\mathbf{k}, \mathbf{k}_i)$.

Electrons, on the other hand, are elastically scattered within a few topmost atomic layers. Also in this case, there is no strict selection rule for \mathbf{k}_\perp such that the reciprocal lattice in a LEED experiment is well described by lattice rods, similarly to helium atom scattering. However, the finite penetration depth of the electrons and multiple scattering events vary the structure factor as a function of \mathbf{k}_i and \mathbf{k}_f . The intensity distribution along the lattice rods is therefore strongly modulated.

Also for low-energy electron diffraction, the approximation of the complete scattering event as a single scattering process is useful for different purposes of analysis. Within the kinematic approximation, all form factors $f_n(\mathbf{k}, \mathbf{k}_i)$ are substituted by an averaged form factor $f(\mathbf{k}, \mathbf{k}_i)$. (This approximation implies also the negligence of steps as the atomic configurations in their surrounding are clearly different). Extracting these factors from the summation, the intensity $I(\mathbf{k}, \mathbf{k}_i)$ splits up into two factors

$$I(\mathbf{k}, \mathbf{k}_i) = |\psi(\mathbf{k}, \mathbf{k}_i)|^2 = F(\mathbf{k}, \mathbf{k}_i)G(\mathbf{k}) \quad (3.11)$$

with the dynamical form factor

$$F(\mathbf{k}, \mathbf{k}_i) = |f(\mathbf{k}, \mathbf{k}_i)|^2 \quad (3.12)$$

and the lattice factor,

$$G(\mathbf{k}) = \sum_{n,m} e^{i\mathbf{k}(\mathbf{r}_n - \mathbf{r}_m)} . \quad (3.13)$$

While the dynamical form factor $F(\mathbf{k}, \mathbf{k}_i)$, depending on the initial and final wave vector, provides information about the arrangement of atoms within the unit cell and multiple scattering effects, the lattice factor $G(\mathbf{k})$, as the Fourier transform of the lattice, yields information about the arrangement of unit cells. The latter therefore does not modify the integral intensity of the diffraction spots ij

$$\int_{BZ} G_{ij}(\mathbf{k}) d\mathbf{k}_\parallel = 1 . \quad (3.14)$$

This is of particular importance for the practical spot profile analysis.

3.2 Helium Atom Scattering (HAS)

As described previously, elastic helium atom scattering probes the corrugation function and therefore is only sensitive to the topmost layer of the sample. This, in addition to the large scattering cross section of all kinds of adatoms (and defects) makes Helium scattering an ideal technique to study growth processes on surfaces. Furthermore, the He beam does not influence the surface structure and consequently is absolutely non-destructive.

3.2.1 Beam Generation

The crucial part in atom scattering experiments is to obtain a highly monochromatic beam with a good energy as well as angular resolution in order to achieve a large transfer width. The He beam is produced by a high pressure supersonic expansion source (nozzle pressure 10-100 bar, nozzle diameter 5-10 μm). The Maxwellian velocity distribution of the He atoms behind the nozzle is significantly narrowed and the mean velocity is enhanced by a factor of 5/3 [48], thus leading to

$$E = \frac{1}{2}mv_0^2 = \frac{5}{2}k_B T_0 \quad (3.15)$$

where v_0 denotes the average velocity of the particles and T_0 the nozzle temperature. The speed ratio S defined as

$$S = \sqrt{\frac{\frac{1}{2}mv_0^2}{k_B T}} = \sqrt{\frac{5T_0}{2T}} \quad (3.16)$$

where T is the temperature associated to the thermal motion of the He atoms in the beam, yields a good characterization for nozzles used in supersonic beam expansion as the velocity distribution is then given by [48]

$$\frac{\Delta v}{v_0} \approx \frac{1.65}{S} \quad (3.17)$$

Since S increases with stagnation pressure p_0 and nozzle diameter d as $S \propto (p_0 d)^\beta$ with β in the range of 0.4-0.545 [49, 50], and the nozzle flux F as $F \propto p_0 d^2$, a large stagnation pressure at small nozzle diameter is preferred. However, the flux is limited by the available pumping speed. Typical experimental values are listed in table 3.1.

3.2.2 Scattering Geometry

The highly monochromatic helium beam generated in the source chamber is collimated by a skimmer and then directed through an aperture into the scattering chamber onto the sample. The scattered beam is detected under a total scattering angle of 90° by a quadrupole mass spectrometer. As the initial and final wavevector and the surface normal are located in a common plane, the geometry is called in-plane scattering. The parallel momentum transfer is varied by rotating the sample around the normal of the scattering plane

$$\Delta k_{\parallel} = k_i(\sin \theta_f - \sin \theta_i) . \quad (3.18)$$

The fixed angle between initial and final wavevector results in probing a ‘modified’ Ewald sphere centered at (000) with radius $r = \sqrt{2}k_i$ (sketched in figure 3.3(b)).

As mentioned earlier, a large stagnation pressure is required to obtain suitable He beam properties. This imposes a great challenge on the vacuum system, such that not only the

Source	Nozzle diameter	$5 \mu\text{m}$
	Nozzle pressure	$\leq 100 \text{ bar}$
	Nozzle temperature	30-300 K
	He beam energy	10-65 meV
	He beam velocity	600-1800 m/s
	Relative velocity spread ($\Delta v/v_s$)	$\geq 1 \%$
Dimensions	Source-aperture distance (D_{SA})	14.2 cm
	Source-sample distance (D_{SS})	50 cm
	Sample-detector distance (D_{SD})	79.8 cm
	Source-target-detector angle (fixed)	$(90 \pm 0.25)^\circ$
Detector	Ionization volume	$(15 \times 7.5 \times 11) \text{ mm}^3$
	Channel width MCA	$1 \mu\text{s}$
	Dynamic range	$\sim 5 \times 10^5$
Resolution	Polar angle	$\sim 0.25^\circ$
	Energy resolution	$\sim \pm 0.2 \text{ meV}$
	Transfer width	$\leq 120 \text{ \AA}$
Pressure	Source (expansion) chamber (beamI)	10^{-7} mbar (without helium) 10^{-4} mbar (with helium)
	Chopper chamber (beamII)	10^{-8} mbar (without helium) 10^{-6} mbar (with helium)
	Sample chamber	10^{-10} mbar (without helium) 10^{-9} mbar (with helium)
	Detector chamber	10^{-10} mbar (without helium) 10^{-10} mbar (with helium)

Table 3.1: A list of important experimental parameters for the Helium scattering apparatus.

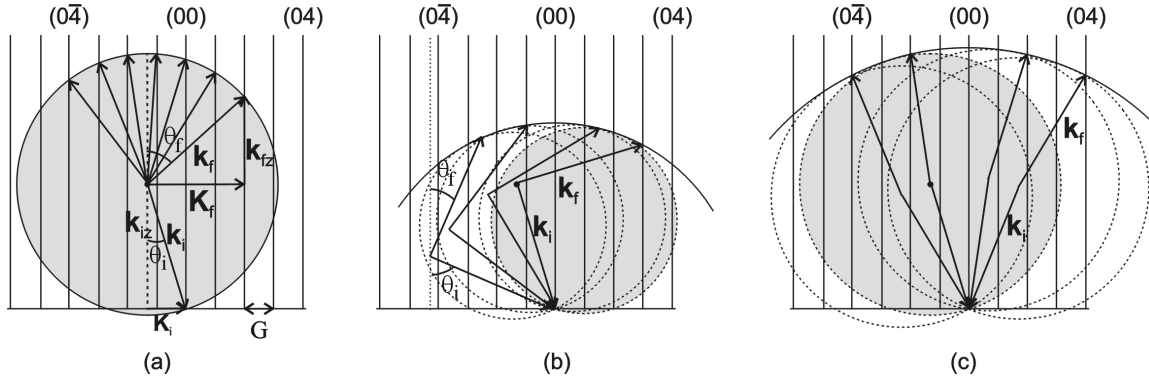


Figure 3.3: (a) Conventional Ewald sphere construction. (b, c) The modified Ewald sphere construction for a constant angle between initial and final wave vector corresponding to the scattering geometry in Helium atom scattering and SPA-LEED, respectively. In the HAS chamber the source and detector position are fixed, enclosing a total scattering angle of 90° (b), while the electron gun and channeltron are separated by 4° in the SPA-LEED apparatus (c).

pumping speed in the beam generation part must be of high power but also in the scattering chamber and especially in the detector unit. Therefore, the detector arm is pumped by three differential pumping stages. An illustration of the helium beam passing through the experimental chamber is shown in figure 3.4.

3.2.3 Transfer Width

In a diffraction experiment the resulting diffraction pattern is the superposition of the interference patterns of each individual particle. As any real instrument exhibits an energy and angular spread, the interference patterns are not all perfectly the same. This leads to an instrumental broadening of the diffraction spots. The transfer width is a measure of this broadening effect. It describes the length on a surface which would lead to the instrumental width of the diffraction spots. Information on length scales larger than the transfer width cannot be obtained. Therefore, the transfer width can be regarded as the resolution limit in a diffraction experiment.

Comsa has investigated the problem of the determination of the transfer width in detail for atom scattering experiments [52]. The first part is the energy spread of the beam, as particles of different energy each contribute to ‘overlapping’ diffraction patterns. This contribution can be written as [52]

$$w_E \approx \frac{\lambda}{|\sin \Theta_i - \sin \Theta_f| \sqrt{(\Delta E_0)^2 / E_0^2}} \quad (3.19)$$

where $(\Delta E_0)^2$ is the mean squared energy spread of the beam with primary energy E_0 and

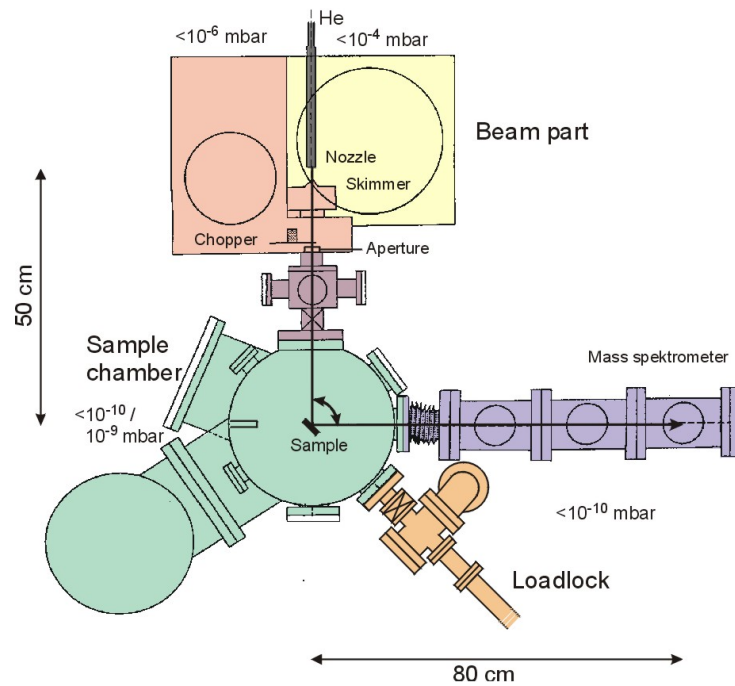


Figure 3.4: Illustration of the helium atom scattering chamber [51]. The He beam is generated by supersonic free jet expansion in the source chamber, directed through a skimmer and a collimator aperture onto the sample in the scattering chamber. Under a total scattering angle of 90° the diffracted beam is detected by a mass spectrometer.

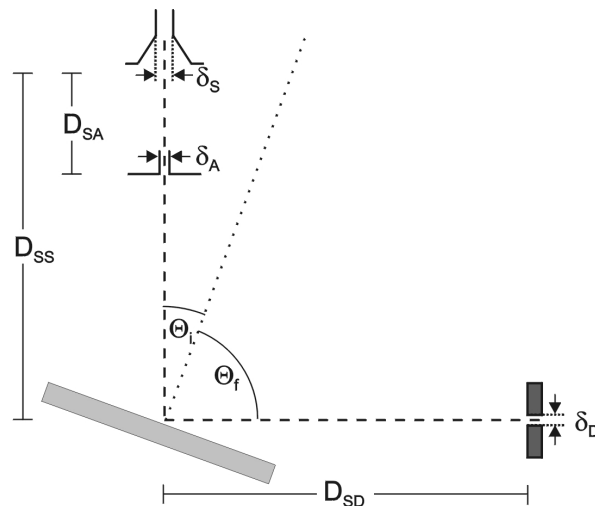


Figure 3.5: Schematic scattering geometry: δ_S , δ_A , δ_D denote the diameter of the skimmer, the beam collimator aperture, and the detector aperture, respectively, and D_{SA} , D_{SS} , and D_{SD} the distance skimmer - beam collimator aperture, skimmer - sample, and sample - detector, respectively.

wavelength λ .

Secondly, a geometrically derived contribution to the transfer width was determined by Comsa to [52]

$$w_{\Theta} = \frac{\lambda}{|\Delta\Theta_f| \cos\Theta_f} \quad (3.20)$$

with

$$(\Delta\Theta_f)^2 = \left(\frac{\cos\Theta_i}{\cos\Theta_f} \frac{\delta_S}{D_{SS}} \right)^2 + \left(\frac{\cos\Theta_i}{\cos\Theta_f} \frac{\delta_A}{D_{SA}} \right)^2 + \left(\frac{\cos\Theta_f}{\cos\Theta_i} \frac{D_{SA}}{D_{SD}} \frac{\delta_A}{D_{SA}} \right)^2 + \left(\frac{\delta_D}{D_{SA}} \right)^2 \quad (3.21)$$

for which the corresponding aperture widths and distances are indicated in figure 3.5. The resulting total transfer width $w = \sqrt{w_{\Theta}^2 + w_E^2}$ thus yields

$$w \approx \frac{\lambda}{\sqrt{(\Delta\Theta_f)^2 \cos^2\Theta_f + (\sin\Theta_i - \sin\Theta_f)^2 (\Delta E_0)^2 / E_0^2}}. \quad (3.22)$$

The transfer width of the HAS chamber used can thus be calculated to amount to a maximum of 120 Å at $\Theta_i = 45^\circ$ and smaller values at other angles.

3.2.4 Diffuse Scattering of Adsorbates

In addition to the study of diffraction from ordered surfaces HAS is frequently used to investigate disordered systems such as adsorption and defects on surfaces. The physical reason for this capability lies in the large scattering cross section for He of individual scatterers causing diffuse scattering over an area Σ (up to several hundred Å²). A significant decrease in specular intensity occurs for defect coverages down to ≈ 0.001 monolayers. Since the specular peak profile is independent of the presence of adsorbates, the peak height itself is a measure of the intensity [53].

At very low coverages, the specular scattered intensity arises exclusively from the undisturbed substrate area [54]. Quantitatively, the decrease in specular intensity due to diffuse scattering can then be described by

$$1 - I/I_0 = n\Sigma = n_s\theta\Sigma \quad (3.23)$$

where $\theta = n/n_s$ and n, n_s denote the number of adsorbates and substrate atoms per unit area, respectively. Differentiation of equation 3.23 yields [53]

$$\Sigma = -\frac{1}{n_s} \frac{d(I/I_0)}{d\Theta} \Big|_{\Theta=0}. \quad (3.24)$$

Thus, the scattering cross section can be derived from the initial slope of an adsorption curve. With a known cross section of the adsorbate, the coverage can be determined as will be done in chapter 5.

As the adsorption proceeds, the scattering cross sections start to overlap and the relative specular intensity is given by [54]

$$I/I_0 = (1 - \theta)^{\Sigma n_s} \quad (3.25)$$

if the adsorbates are randomly distributed perfectly diffuse scatterers. In case of island growth a linear decrease is expected [45].

3.3 Spot-Profile Analyzing Low-Energy Electron Diffraction (SPA-LEED)

3.3.1 Scattering Geometry

The advantage of a SPA-LEED apparatus over a conventional LEED set-up is its increased resolution and in consequence the possibility of spot profile analysis. The transfer width of the used commercial Omicron SPA-LEED amounts to about 1000 Å (the transfer width of a conventional LEED set-up is one order of magnitude smaller).

In order to obtain such a large transfer width a finely focused electron beam with low energy spread and an appropriate detector are required. The specialty of the scattering geometry is illustrated by the schematic set-up of the SPA-LEED unit in figure 3.6. The path of the incident as well as outgoing electrons is controlled by an octupole deflection unit. The diffracted electrons are detected by a single electron channeltron detector allowing for a dynamic range of 10^6 . By changing the voltage at the deflection unit the angle of the incident electrons is varied which simultaneously results in a variation of the angle under which the diffracted electrons are detected. The angle between the incident and final scattering vectors remains constant at 4° which is the separation angle between electron gun and channeltron. This characteristic scattering geometry results in probing a ‘modified’ Ewald sphere (similarly as in the HAS apparatus and sketched in figure 3.3(c)), which is centered at the origin (000) and has a radius of

$$r = 2k_i \cos \frac{\theta}{2} \quad (3.26)$$

with θ the angle between electron gun and channeltron.

3.3.2 Spot Profile Analysis

Length scales of rough surfaces can be determined by an analysis of the spot profile $I(\mathbf{k}_{\parallel})$ if they are smaller than the instrumental transfer width. When the scattering occurs at adjacent terraces with a height difference, the final wave functions are shifted with respect to each other. Denoting the phase difference in numbers of particle wavelength λ by S , constructive interference

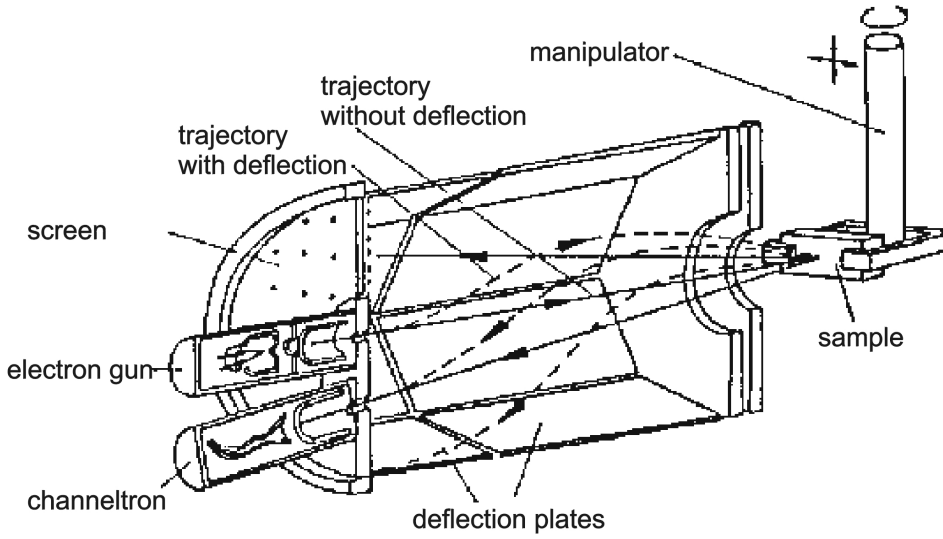


Figure 3.6: Schematic SPA-LEED set-up from [55]: the electron gun, the channeltron detector, the deflection unit, and the sample position are indicated. The path of the electrons from the gun to the detector is illustrated. The angle of incidence is varied by the voltage at the octupole deflection unit. The spot position on the sample remains constant during scanning.

takes place for integer values of S . In this case, diffraction is not sensitive to surface roughness, but for out-of-phase conditions, i.e., destructive interference, the diffraction experiment is most sensitive to surface morphological features. For a multilevel system, the full-width at half-maximum (FWHM) of the diffraction peaks is given by [56]

$$FWHM = \frac{\pi(1 - \cos(2\pi S))}{\bar{T}} \quad (3.27)$$

with \bar{T} as the average terrace width.

It should be noted that thermal effects, i.e., inelastic scattering at vibrational lattice modes, do not contribute to a diffraction spot broadening but to a reduction in intensity and therefore increase the detected background.

3.3.3 Representation of SPA-LEED Images in \mathbf{k} -space

As the voltage at the deflection unit determines the angle of incidence and finally the parallel momentum transfer of the detected electrons, the SPA-LEED images can easily be mapped into \mathbf{k} -space. However, for large voltages, non-linearities in the deflection unit distort the recorded patterns. On the basis of known \mathbf{k}_{\parallel} values, the images can be re-scaled [57].

Besides the usual \mathbf{k}_{\parallel} images, i.e., diffraction patterns at constant energy, \mathbf{k}_{\perp} vs. \mathbf{k}_{\parallel} scans are directly accessible by recording a set of line-scans along a particular \mathbf{k}_{\parallel} -direction at varying energy. Equivalent to the 2D diffraction patterns, the \mathbf{k}_{\parallel} value is determined by the voltage applied at the deflection unit. Hence, the lattice rods of the surface run perpendicular in this representation. Facet structures can thus be resolved easily [58], as their lattice rods are inclined with respect to those of the macroscopic surface and the angle of inclination can directly be taken from such a type of scan.

Moreover, this representation is useful for the determination of step heights, since in- and out-of phase conditions can directly be observed.

3.4 Low Energy Electron Microscopy

A low-energy electron microscope provides the unique opportunity to study surface morphologies and structures with a spatial resolution on the nm-scale and video-rate time resolution.

3.4.1 LEEM Instrumentation

Figure 3.7 shows a schematic diagram of the LEEM in the group of Prof. Horn-von Hoegen, where the experiments were carried out. A brief summary of the most important features of the LEEM imaging technique is reported in the following, while details of this instrument can be found in publications by Tromp and Reuter [59, 60].

The basis for this technique is the use of the diffracted low energy electron beams for imaging the real space of a surface. One difficulty in the experimental set-up is the separation of the incident and outgoing electron beams, as the incident beam has to be normal to the sample surface. In the depicted apparatus this problem is solved by introducing a 120° magnetic deflection unit (sector field) in front of the objective lens and the sample. The electrons emitted from an electron gun are focused by a set of lenses and directed through the sector field onto the sample. The reflected electrons again pass the sector field to reach the projector column. Upon impinging on the sample the electrons have kinetic energies between 0 eV and about 100 eV. Since electrons of high energy are more easily focused and higher resolution can be achieved, the electron beam is not transported at low energies, but at 15 keV. The sample potential is held at high voltage to decelerate the incident beam to the desired low energy and to accelerate the reflected electrons back to high voltage. The objective lens, located between sample and sector field, is kept on ground potential.

In order to compensate exterior magnetic fields, such as the earth's field, a set of Helmholtz coils is used around a cage, in which the microscope is placed.

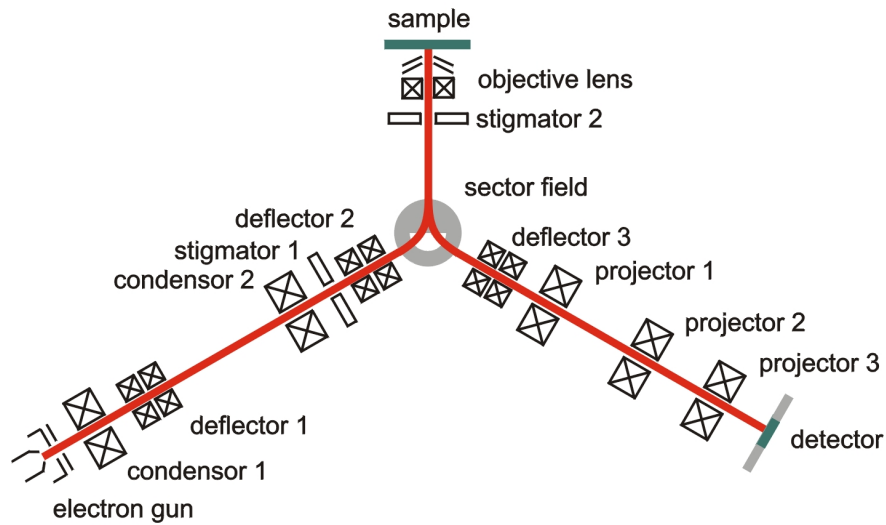


Figure 3.7: Schematic LEEM set-up: The left part of the figure illustrates the electron gun column, in which the electron beam is directed into the sector field and from there perpendicular onto the sample. The reflected electron beam again passes the sector field and reaches the imaging column on the right hand side of the figure.

3.4.2 Imaging with LEEM

The complete process to obtain an image by LEEM can be divided into two parts. First, the illumination of the sample and second, the imaging of the reflected electrons.

Sample Illumination

The electron beam, being generated by an electron gun, illuminates a spot of $5\ \mu\text{m}$ to $50\ \mu\text{m}$ in diameter on the sample. The size of this area can be varied by changing the gun focus in combination with the focal length of the first condenser lens. The second condenser lens then transfers the beam focus to the back focal plane of the objective lens, which then transmits the beam onto the sample. Consequently, the surface is perpendicularly illuminated by a collimated, coherent electron beam.

Objective Lens

If the electrons are scattered from a long-range ordered surface, they form a diffraction pattern in the back focal plane of the objective lens. Figure 3.8 illustrates the common feature of all lenses to simultaneously image the real and reciprocal space. While the real image of an object outside the focal distance is usually constructed by rays originating from a common point, the

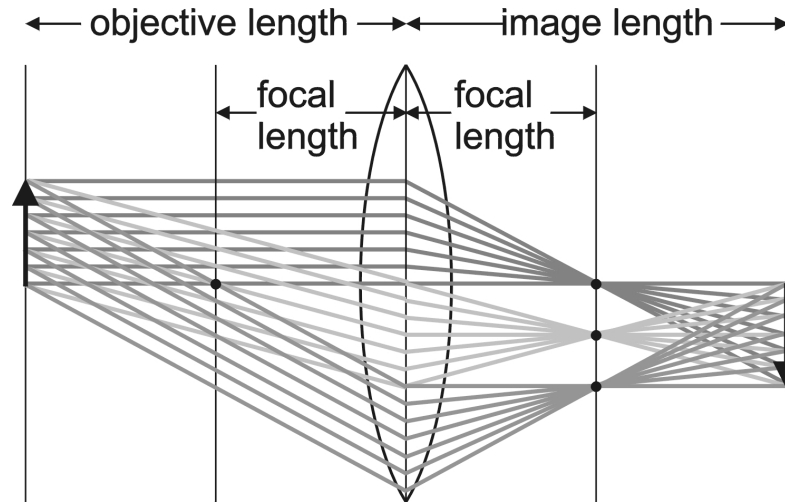


Figure 3.8: Ray diagram for a conventional lens: Rays leaving the object under a common angle but from different origins coincide in the back focal plane.

formation of the diffraction pattern is illustrated by a set of rays starting at different locations of the object. Rays of common angle are then shown to coincide in the back focal plane of the lens. Since constructive interference of the waves occurs under special angles, where the Bragg condition is satisfied, the diffraction pattern is found in the back focal plane of the objective lens. While the back focal plane sorts rays by angle, rays of common origin again meet in the image plane.

Imaging Column

The first image of the sample (20 times magnified) is formed at the center of the sector field. Projector 1 transfers the image onto its image plane. The focal length of projector 2 can be varied to either image the diffraction pattern or the real image of the first projector. The combination of projector 2 and 3 magnifies the image or the diffraction pattern onto a channel plate intensified phosphor screen, from where it is recorded on video tape.

Projector 3 consists of two identical, coupled lenses which are controlled by an equal but opposite lens current such that the combination operates without rotation. Hence, only the lens current of projector 2 rotates the image. However, the images' orientation with respect to the structural symmetry can be derived by a comparison of the lens' currents during real space and diffraction pattern imaging.

3.4.3 Contrast Mechanisms

The LEEM set-up provides a couple of contrast mechanisms as briefly reviewed in the following.

Mirror Electron Microscopy (MEM)

In mirror electron microscopy mode (MEM) the sample potential is held slightly higher than the electron gun potential. Thus, the electrons are reflected in front of the sample, which can then be regarded as an electron mirror. Image contrast in this mode is based in topographic roughness as well as local differences in the electrostatic potential due to variations in work function.

Phase contrast between surface structures of different work functions can be achieved if the electron kinetic energy is set such that the majority of the electrons is reflected in front of the surface structure of higher work function, while they can penetrate into the surface area of lower work function. Due to scattering effects within the sample, a considerable part of the electrons cannot leave the sample anymore. The reflected intensity is therefore strongly decreased.

In addition to the work function contrast, steps on the surface can be imaged. However, it should be noted that it cannot be distinguished between a step in the electrostatic potential or in topography. The reflected electrons from a lower terrace travel a longer path than those reflected from an upper terrace resulting in a phase difference in the electron plane waves reflected from both. If the objective lens is slightly defocused, these phase shifted plane waves can be made to interfere in the object plane of projector 1, thus giving rise to Fresnel fringes in the final image [61].

Bright-Field LEEM

If the sample potential is reduced such that the electrons hit the sample, these are diffracted and a LEED pattern appears in the back focal plane of the objective lens while the first real image is found in the center of the sector field, as previously described. Since this image lies in the object plane of the transfer lens (projector 1), the diffraction pattern is also found in the back focal plane of this lens. Here, a contrast aperture can be inserted in order to block all but a selected diffraction spot for image formation. If the (0,0) spot is chosen, the imaging mode is called bright-field LEEM. Contrast arises from differences in the (0,0) spot intensity of different structures, determined by the LEED structure factor. As the difference in intensity depends on the kinetic electron energy, also the magnitude and the sign of the contrast is energy dependent.

Dark-Field LEEM

While in bright-field imaging the (0,0) spot was chosen to form a real space image of the sample, selecting any other diffraction spot by the contrast aperture leads to the so-called dark field imaging mode. If areas of different structure coexist on the sample, selecting a diffraction spot associated to one structure results in an image solely of this structure, while all other areas remain dark (therefore ‘dark-field’ imaging). The advantage of this method is to directly relate the LEEM contrast to the corresponding symmetry.

For the quasicrystal investigations in this thesis, this contrast mechanism was not used. Although different quasicrystalline structures were imaged, the observed diffraction spots were common to all of them.

LEED

Previously, the diffraction pattern of the sample surface was used to image the surface’s real space. If the focal length of projector lens 2 is set such that its object plane coincides with the back focal plane of projector lens 1 the diffraction pattern itself is imaged.

In contrast to conventional LEED where the diffraction spots move towards the (0,0) spot with increasing energy the positions of the diffraction spots in this instrument do not change with energy [62]. This can be seen from the diffraction condition

$$\sin \alpha_0 = \lambda_0 \mathbf{G} \quad (3.28)$$

where α_0 , λ_0 and \mathbf{G} denote the scattering angle from the sample normal, the wavelength and a surface reciprocal vector, respectively. The electrons are then accelerated in the electric field between the sample and the objective lens to $E_1 = 15 \text{ keV}$. The corresponding wavelength λ_1 and angle α_1 are related by Snellius’ law to the original values

$$\frac{\sin \alpha_0}{\lambda_0} = \frac{\sin \alpha_1}{\lambda_1} . \quad (3.29)$$

Combination of these equations yields

$$\sin \alpha_1 = \lambda_1 \mathbf{G} \quad (3.30)$$

Hence, α_1 is not dependent on the initial wavelength λ_0 , but only on \mathbf{G} . From figure 3.8 it can be inferred that the distance r from the center of the back focal plane to a particular diffraction spot is given by

$$r = f \tan \alpha_1 \quad (3.31)$$

with f being the focal length. Consequently, the location of the diffraction spot in the back focal plane is not energy dependent.

Thus, the size of the Ewald sphere increases with energy, but the diffraction spots remain in their location. This makes it easy to identify facets, since their diffraction spots move with varying energy.

3.5 Sample Preparation

The investigated quasicrystal samples can be grouped into three classes. One comprises samples from the decagonal Al-Ni-Co system. They were grown by the Czochralski method [4, 5], cut either perpendicular to the tenfold $[00001]$ -axis, the twofold $[10000]$ -axis, or the twofold $[001\bar{1}0]$ -axis. While the samples used for the growth experiments in the HAS and SPA-LEED apparatus were of the composition $\text{Al}_{71.8}\text{Ni}_{14.8}\text{Co}_{13.4}$, the LEEM experiments were mainly carried out on $\text{Al}_{72.3}\text{Ni}_{9.5}\text{Co}_{18.2}$ samples. All these were provided by Prof. Dr. Peter Gille from the Ludwig-Maximilians-Universität, München.

The second class constitutes the icosahedral $\text{Al}_{70.5}\text{Pd}_{21}\text{Mn}_{8.5}$ sample, which was grown by the Czochralski method and then annealed at 800°C for three months [6, 63, 64]. This was only used with its fivefold axis aligned parallel to the surface normal and provided by Dr. Philipp Ebert from the Institut für Festkörperforschung, Forschungszentrum Jülich.

All samples were polished with diamond paste. After insertion of the samples into the UHV chambers, they were cleaned by cycles of ion bombardment (Ne^+ , 1-5 keV) and annealing at about 850°C in case of the Al-Ni-Co samples and about 650°C for the Al-Pd-Mn samples.

Deposition of Sb, Bi and As was carried out by use of an electron beam evaporator.